High-resolution ^{1}H NMR of powdered solids by homonuclear dipolar decoupling

Federico M. Paruzzo, Lyndon Emsley *

Institut des Sciences et Ingénierie Chimiques, École Polytechnique Fédérale de Lausanne (EPFL), 1015 Lausanne, Switzerland

ARTICLE INFO

ABSTRACT

The development of homonuclear dipolar decoupling sequences to obtain high-resolution ^{1}H NMR spectra from solids has recently celebrated its 50th birthday. Over the years, a series of different decoupling schemes have been developed, starting with the pioneering Lee-Goldburg and WAHUHA sequences up to the most recent generation of experimentally optimized phase-modulated schemes such as eDUMBO-1$_{22}$ and LG4. These schemes can all yield over an order of magnitude reduction in ^{1}H NMR linewidths in solids. Here we provide an overview and a broad experimental comparison of the performance of the main sequences, which has so far been absent in the literature, especially between the newest and the oldest decoupling schemes. We compare experimental results obtained using eight different decoupling schemes (LG, WHH-4, MREV-8, BR-24, FSLG/PMLG, DUMBO-1, eDUMBO-1$_{22}$ and LG4) on three different microcrystalline powdered samples (alanine, glycine and β-AspAla) and at three different MAS rates (3.0, 12.5 and 22.0 kHz). Finally, since these sequences can be technically demanding, we describe the experimental protocol we have used to optimize these schemes with the aim to provide simple guidelines for the optimization of CRAMPS experiments for all NMR users.

1. Introduction

Just over 50 years ago, the pioneering works of Lee and Goldburg [1,2] and Waugh and co-workers [3] revolutionized the world of solid-state nuclear magnetic resonance (NMR) with the introduction of the Lee-Golburg (LG) and WAHUHA (WHH-4) pulse sequences respectively. Following the principles of coherent averaging [4], these pulse sequences can remove the broadening effects of homonuclear dipolar couplings in solid samples, while leaving the chemical shift interactions (at least partially) intact. The dramatic line narrowing effect was first demonstrated for WHH-4 with the ^{19}F spectrum of a single crystal of CaF$_2$ as reproduced from the original article in Fig. 1. Despite their technical differences, both LG and WHH-4 work in a very similar way: they generate a rotation of the spin operators in the spin space around an effective field tilted of 54.74° with respect of the main static magnetic field. This rotation is achieved with a continuous off-resonance irradiation in the case of LG, and with four π/2 pulses in the case of WHH-4. The result is that the homonuclear dipolar coupling is averaged to zero (to first order), in a manner similar to that achieved by magic angle sample spinning (MAS) [5,6], while

the chemical shift interaction is only scaled by a factor of $1/\sqrt{3}$. Another way to do this was demonstrated with the idea of a "magic-echo" in which a burst of radiofrequency irradiation produces a (partially) time reversed dipolar interaction, and which then leads to the formation of a dipolar echo at some time later [7].

While the introduction of LG and WHH-4 was a conceptual landmark, there were two key roadblocks to obtaining truly high-resolution ^{1}H NMR spectra of solids. First, in static samples, the anisotropy of the chemical shift remains. In certain cases this can be useful, but in general one would like to acquire spectra from powders with only isotropic shifts. A solution to this is to combine MAS and multi-pulse spectroscopy, in the so-called CRAMPS approach, introduced in 1977 by Gerstein et al. [8]. As long as the decoupling sequence and the sample rotation do not interfere, CRAMPS leads to a double averaging process that yields ^{1}H spectra with significantly better resolution than MAS alone (at least so far up to MAS rates of 65.0 kHz [9–13]).

The second roadblock is due to the fact that both LG and WHH-4 only lead to removal of the dipolar coupling under ideal conditions to first order. Even if this means that residual broadening might be only about 1% of the initial width (a remarkable achievement), this would lead to residual linewidths in the early work on the order of ~500 Hz (e.g. 1 ppm at 500 MHz), which still severely limits the applicability to complex chemistry. Thus, from these very first

---
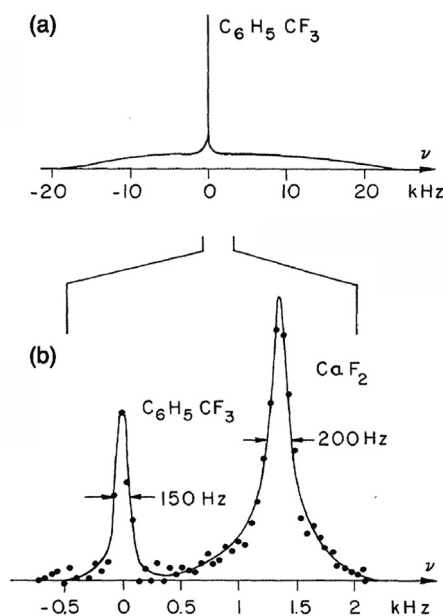
Fig. 1. First example of the performances of homonuclear dipolar decoupling sequences. (a) ^{19}F spectrum of a single crystal of CaF_2 wet with liquid $C_6H_5CF_3$. (b) ^{19}F spectrum of the same compound obtained decoupling the ^{19}F-^{19}F dipolar couplings using WHH-4. Figure adapted with permission from Ref. [3].

developments, the acquisition of ^1H spectra in solids with better resolution has been a challenge faced by many, and which still remains partially unresolved (so to speak).

Using concepts of coherent averaging the WHH-4 and LG blocks were rapidly combined with concepts such as cyclic decoupling and reflection symmetry [14,15] to develop decoupling sequences with better decoupling efficiency. WHH-4 led to MREV-8 in the 1970s [14,63], while the combination of LG with symmetry properties led to flip-flop Lee-Goldburg (FFLG) [16].

The introduction of the CRAMPS experiment then led the development of schemes such as BR-24, BR52 [15] and BLEW12 [17] using WHH-4 as the basic building block, while LG was developed into FSLG [18], which was later implemented as PMLG [19], and LG4 [20,21]. In addition to these, many other schemes were developed aiming at better decoupling. For example, extensive analysis of the terms composing the dipolar Hamiltonian with average Hamiltonian theory [4] and their symmetry properties led to the so-called high order truncation (HOT) multiple pulse techniques, such as MSHOT-3 [22,23]. Another elegant example of symmetry considerations applied in the development of decoupling schemes was introduced by Levitt with the development of the rotor synchronized RN_n^ν sequences [24].

A different approach was used for the development of another class of decoupling sequences: the so-called decoupling using mind-boggling optimization (DUMBO) family. These were sequences developed using numerical optimization of continuous phase-modulated radiofrequency (rf) irradiation schemes based on either numerical simulations (DUMBO-1 [25]) or direct experimental optimization (eDUMBO-1$_{12.5}$ and eDUMBO-1$_{22}$ [26]).

Finally, we note that when dealing with high-abundance and high-gyromagnetic ratio nuclei such as ^1H, CRAMPS experiments are extremely powerful tools, especially in the low to moderate regime of MAS where chemical shift information is otherwise inaccessible. However, these experiments are still comparatively rarely used in routinely NMR analysis, perhaps because they have acquired a reputation of being technically very demanding. Indeed, with the technology of NMR consoles and rf amplifiers of the 70–90s, implementing homonuclear dipolar decoupling was an art in

itself, requiring careful optimisation along the whole chain of spectrometer components [27–31]. However, with the introduction of modern digital NMR spectrometers at the beginning of this century and the development of reliable high-performance routine MAS probes, there are no longer any significant technical challenges associated in implementing these pulse sequences.

This work aims to make homonuclear dipolar decoupling experiments accessible to all NMR users. In this frame, we provide a comparison of CRAMPS experiments using eight homonuclear dipolar decoupling sequences: LG, WHH-4, MREV-8, BR-24, PMLG, DUMBO-1, eDUMBO-1$_{22}$ and LG4. (We note that FSLG and PMLG are formally equivalent. Here we denote the sequence as PMLG in the following). We assess the experimental properties and performances of these schemes through the acquisition of 1D spectra and T'_2 measurements [32] on three different samples (β-AspAla, alanine and glycine (Fig. 2)) and at three different MAS rates (3.0, 12.5 and 22.0 kHz MAS). To our knowledge, this is the broadest experimental comparison of homonuclear dipolar decoupling sequences provided so far using modern NMR spectrometers [9,17,20–22,26,27,33–44]. To facilitate the implementation of these experiments we provide step by step guidelines for their optimization which in principle can be extended to any other homonuclear dipolar decoupling schemes.

2. Materials and methods

The powdered samples of alanine (2-aminopropanoic acid) and β-AspAla ((2S)-2-amino-3-{[(1S)-1-carboxyethyl]carbamoyl}propanoic acid), were purchased from Bachem and Acros Organics. Glycine (2-aminoacetic acid) was found on a shelf. The glycine sample was recrystallized from H_2O to obtain the α form [45]. β-AspAla and alanine were used without further recrystallization.

Experiments were performed on a Ascend 500 wide-bore Avance III HD NMR spectrometer, operating at Larmor frequency of 500.46 MHz for ^1H, equipped with H/X/Y 3.2 mm CPMAS probe. Samples were restricted to the central third of a rotor with inner diameter of 2.2 mm in order to maximize rf homogeneity. This is done by inserting a 12 μl Teflon spacer above the sample and below the drive cap, while in the lower part of the rotor the sample is already restricted by the thick bottom wall of the reduced volume 3.2 mm rotor.

1D ^1H CRAMPS experiments were acquired using the sequences shown in Fig. 3a and b. After the initial π/2 pulse, a θ pulse (the so-called pre-pulse) rotates the magnetization into the tilted transverse plane that will be generated by the effective field of the homonuclear decoupling sequence [21,28,46] and then the FID is sampled in acquisition windows inserted within the homonuclear dipolar decoupling period. Windowed schemes (WHH-4, MREV-8 and BR-24 – Fig. 4b–d) contain delays which allow the insertion of an acquisition window within the decoupling cycle (Fig. 3b) [3,7,14,15,63], while windowless sequences (LG, PMLG, DUMBO-1, eDUMBO-1$_{22}$ and LG4 - Fig. 4a, e–h) necessitate the addition of an extra delay for the signal to be sampled in the absence of rf irradiation (Fig. 3a) [35,47,48]. Note that all the sequences implemented here are implemented in the original versions and not in the z-rotation versions [49,50]. As discussed in Section 4 below,
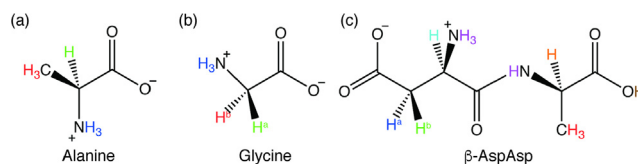
Fig. 2. Chemical formulae of alanine (a), glycine (b) and β-AspAla (c). Hydrogens are colored in order to correspond to the peaks in the spectra that follow.
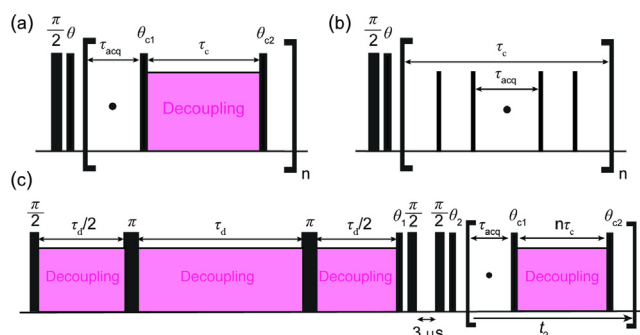
Fig. 3. Pulse sequences used for the acquisition of: (a and b) 1D ^{1}H CRAMPS experiments with windowed (a) and windowless (b) decoupling schemes, and (c) T_2 dephasing curves. Pulse programs and the phase cycles are given in the ESI.
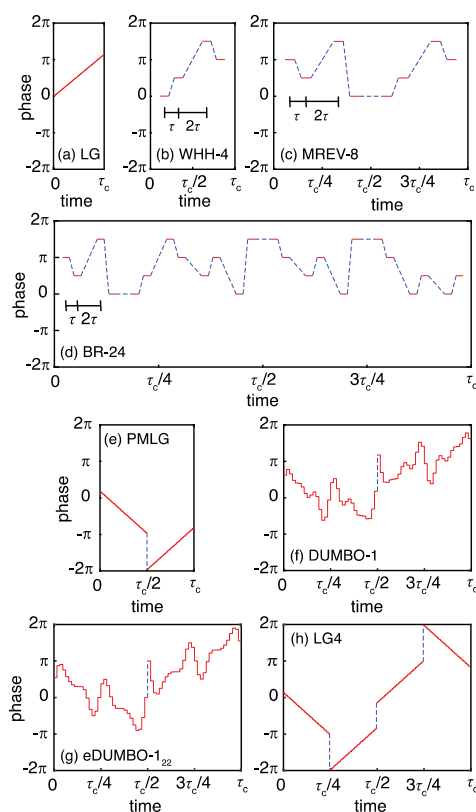
Fig. 4. (a–h) Phase modulation waveforms for LG (a), WHH-4 (b), MREV-8 (c), BR-24 (d) PMLG (e), DUMBO-1 (f), eDUMBO-1$_{22}$ (g), and LG4 (h) decoupling sequences. The width of each plot is proportional to the typical length of the corresponding decoupling cycle. The blue dotted lines indicate phase jumps. Rf irradiation is not present during the phase jumps in WHH-4, MREV-8 and BR-24. (For interpretation of the references to colour in this figure legend, the reader is referred to the web version of this article.)

the z-rotation implementation produces a significant reduction of the scaling factor, and therefore resolution. As a consequence we recommend using sequences that are not supercycled, and where the optimization process described below provides spectra which are equally clean. Also note that the LG, FSLG/PMLG, LG4 and the DUMBO type sequences were all implemented in a phase-modulated fashion. Further details, acquisition parameters, pulse sequences and phase cycles are given in the ESI.

Transverse dephasing times (T_2) [32] were measured using the double spin-echo sequence E_yE_y shown in Fig. 3c [51]. The T_2 measurement was performed through a pseudo-2D experiment, with the acquisition of a series of 1D high-resolution ^{1}H spectra where

the time τ_d of decoupling was systematically increased in a multiple of the decoupling cycle time (τ_c) of the sequence under analysis. The dephasing curves were then obtained by plotting the area under each resonance as a function of the dephasing time ($2\tau_d$). Finally, T_2 values were extracted by fitting the dephasing curves to an exponential decay $S(2\tau_d) = a * \exp(-2\tau_d/T_2)$. The homonuclear dipolar decoupling scheme applied during direct acquisition (t_2) and the corresponding parameters were kept unchanged between T_2 measurements performed at the same spinning rate. We chose to use BR-24 at 3.0 kHz MAS and eDUMBO-1$_{22}$ at 12.5 and 22.0 kHz MAS (for details see ESI). It is critical in these T_2 experiments to calibrate the phase of the homonuclear decoupling sequence under analysis in order to align the plane of the effective field during decoupling to be perpendicular to the magnetization after the first $\pi/2$ pulse [46].

Experiments were carried out using rotor spinning rates (υ_r) of 3.0, 12.5 and 22.0 kHz. The parameters of each homonuclear dipolar decoupling scheme were carefully optimized using the procedure described in Section 4 and Appendix A. This optimization was performed independently at each spinning rate for the three samples. All chemical shifts were referenced to pure liquid tetramethylsilane (TMS) at 0 ppm. Scaling factors were determined experimentally by comparing the peak positions in the decoupled spectra with those obtained with a single pulse experiment under MAS. The comparison was made using the CH$_3$ and NH$_3^+$ resonances for alanine (1.13 and 8.54 ppm), the CH$_3$ and OH resonances for β-AspAla (0.86 and 12.85 ppm) and the CH$_2$ peak at lowest chemical shifts and NH$_3^+$ resonances for glycine (2.3 and 8.0 ppm). The MAS chemical shift values were obtained from the spectrum at 22.0 kHz MAS for alanine, while from glycine and β-AspAla we used values obtained from Refs. [52 and 53] respectively, since their resonances are not all resolved at 22.0 kHz MAS.

The processing of the spectra and the calculation of the scaling factors were done using the Bruker program TopSpin 3.5. Extraction of peak positions and experimental ^{1}H linewidths were done in MATLAB using home-written scripts which make use of the peakfit function [54] (details in ESI). The post-processing procedures for the T_2 measurements (extraction of 1D spectra, evaluation of the area under each peak, fitting and extraction of T_2 value) were also done in MATLAB. Full details of acquisition parameters, phase cycles and pulse sequences are given in ESI.

3. Comparison of decoupling performance

Figs. 5, 6 and 7 show the 1D ^{1}H MAS (a) and ^{1}H CRAMPS (b–f) spectra of alanine, glycine and β-AspAla respectively, obtained with WHH-4, MREV-8, BR-24, LG, PMLG, DUMBO-1, eDUMBO-1$_{22}$ and LG4 at 3.0, 12.5 and 22.0 kHz MAS. Note that the results obtained on the PMLG sequence reflect FSLG performance, as these two sequences are equivalent, except for the way they are implemented at the spectrometer. All the measured linewidths from these spectra are given in Tables S9–S11 for alanine, glycine and β-AspAla respectively.

We immediately see that all the CRAMPS spectra yield a remarkable improvement in resolution as compared to the MAS only spectra. This has also been shown to be the case at 65.0 kHz MAS for DUMBO type [10,11] and PMLG type [9,12,13] schemes if the pulse sequences are adapted slightly. (Note that at 65.0 kHz MAS is sufficiently efficient that the chemical shift scaling factors can be higher than the limit of $1/\sqrt{3}$ imposed if the pulse sequence averages the dipolar couplings to zero to first order [9–13,55]). The improvement in resolution comes at the expenses of sensitivity, which here was reduced by a factor of between 4 and 22, depending on the sequence and the acquisition parameters, compared to the spectra acquired at 22.0 kHz MAS.
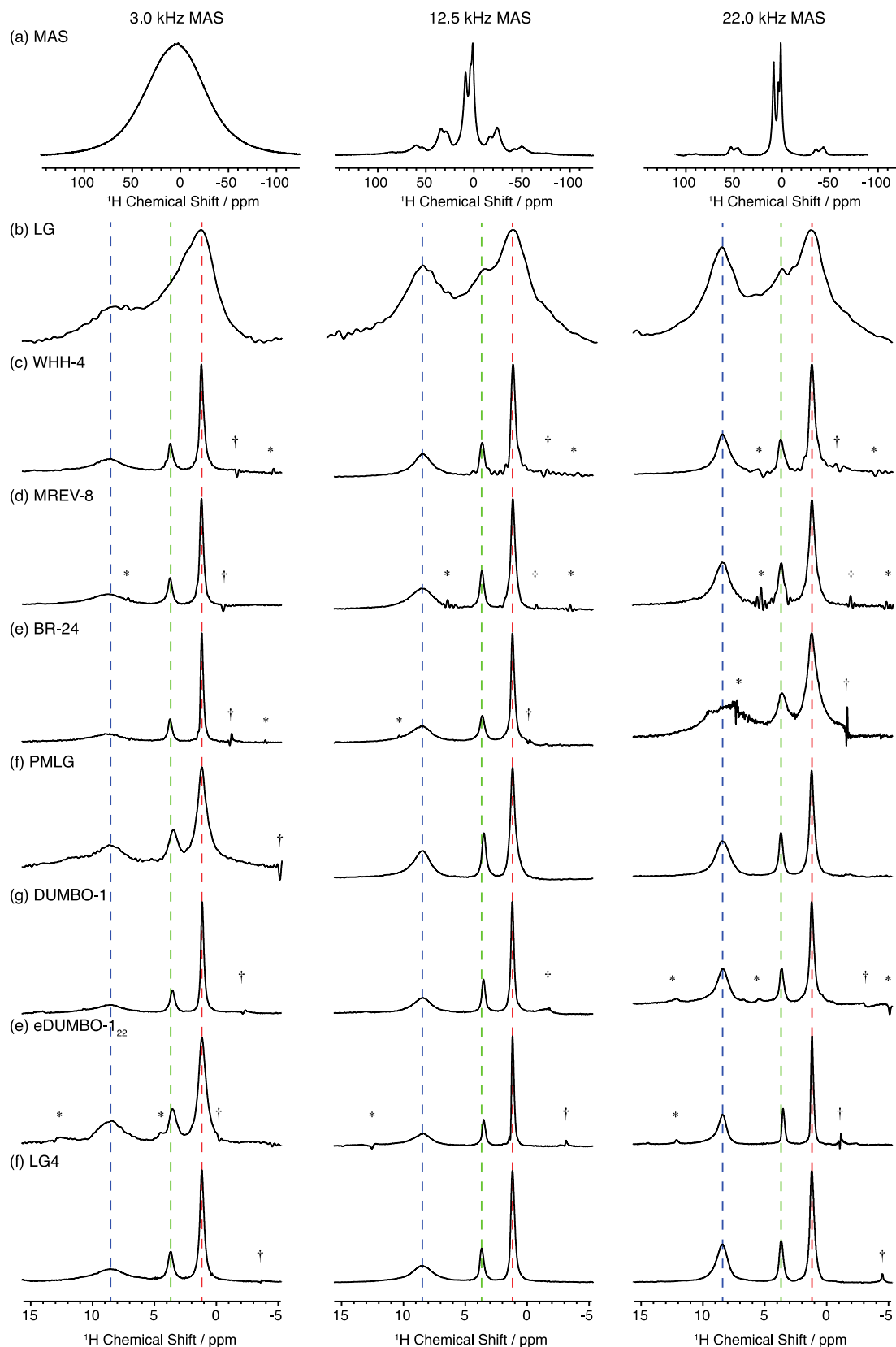
Fig. 5. 1D ^{1}H MAS spectra (a) and 1D ^{1}H CRAMPS spectra (b–i) of powdered alanine. Spectra were obtained decoupling with LG (b), WHH-4 (c), MREV-8 (d), BR-24 (e), PMLG (f), DUMBO-1 (g), eDUMBO-1$_{22}$ (h) and LG4 (i). Spectra in the left, central and right columns were acquired at 3.0, 12.5 and 22.0 kHz MAS rate respectively. Full details on the experimental parameters are given in ESI. Asterisks denote artefacts in the spectra and crosses denote axial peaks. The assignment is done using the color-code of Fig. 1. Spectra are shown after correction for the experimentally measured chemical shift scaling factor, as detailed in the methods section. (For interpretation of the references to colour in this figure legend, the reader is referred to the web version of this article.)
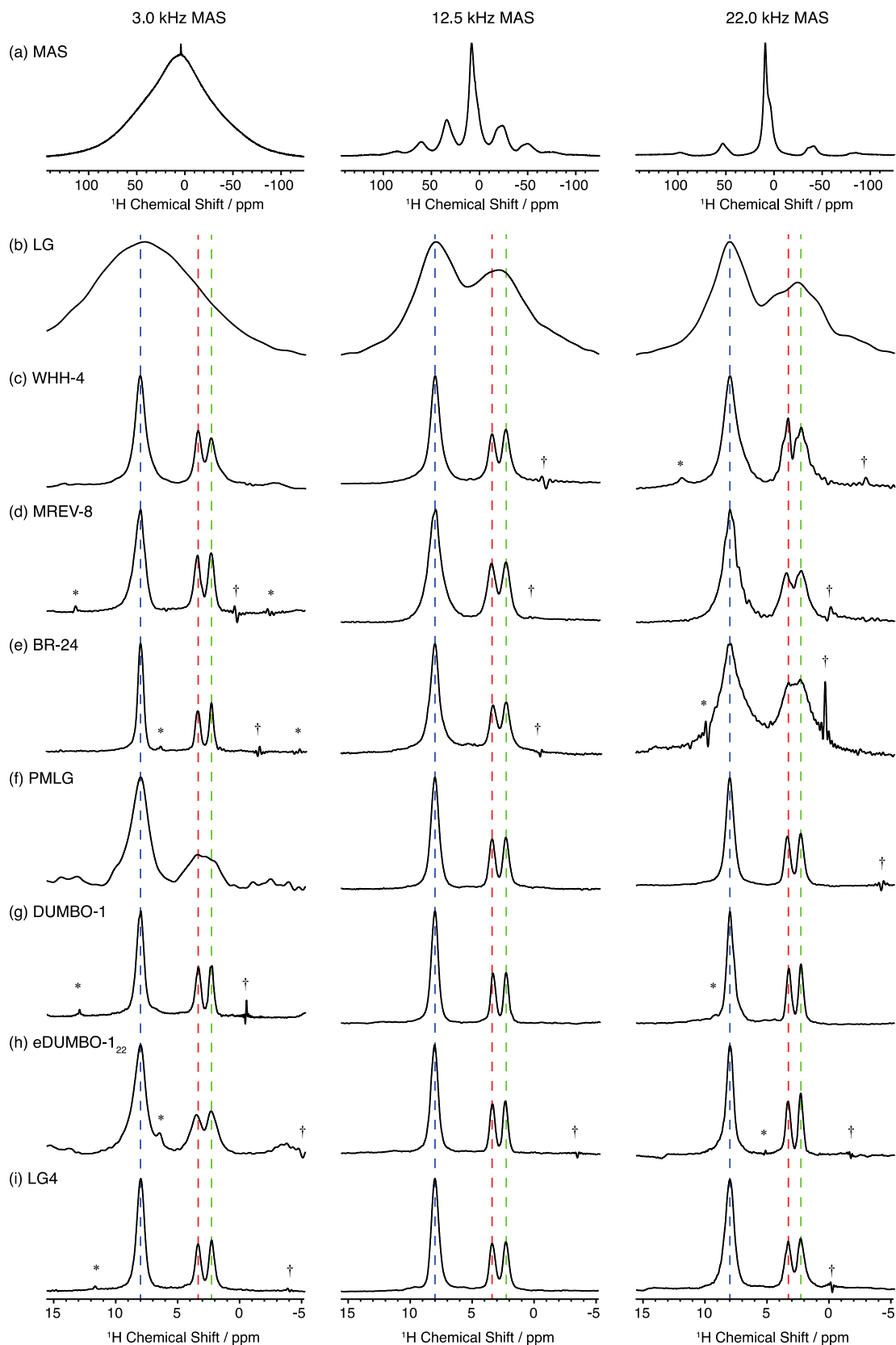
Fig. 6. 1D ^{1}H MAS spectra (a) and 1D ^{1}H CRAMPS spectra (b–i) of powdered glycine. Spectra were obtained decoupling with LG (b), WHH-4 (c), MREV-8 (d), BR-24 (e), PMLG (f), DUMBO-1 (g), eDUMBO-1$_{22}$ (h) and LG4 (i). Spectra in the left, central and right columns were acquired at 3.0, 12.5 and 22.0 kHz MAS rate respectively. Full details on the experimental parameters are given in ESI. Asterisks denote artefacts in the spectra and crosses denote the axial peaks. The assignment is done using the color-code of Fig. 1. Spectra are shown after correction for the experimentally measured chemical shift scaling factor, as detailed in the methods section. (For interpretation of the references to colour in this figure legend, the reader is referred to the web version of this article.)

Fig. 7. 1D ^{1}H MAS spectra (a) and 1D ^{1}H CRAMPS spectra (b–i) of powdered β-AspAla. Spectra were obtained decoupling with LG (b), WHH-4 (c), MREV-8 (d), BR-24 (e), PMLG (f), DUMBO-1 (g), eDUMBO-1$_{22}$ (h) and LG4 (i). Spectra in the left, central and right columns were acquired at 3.0, 12.5 and 22.0 kHz MAS rate respectively. Full details on the experimental parameters are given in ESI. Asterisks denote artefacts in the spectra and crosses denote the axial peaks. The assignment is done using the color-code of Fig. 1. Spectra are shown after correction for the experimentally measured chemical shift scaling factor, as detailed in the methods section.

We also immediately see that the original LG sequence, perhaps not unexpectedly, yields significantly worse results than any of the other sequences across the board.

All three compounds show the same trends. First we see that among the three "first-generation" multiple-pulse sequences (WHH-4, MREV-8 and BR-24) the decoupling efficiency in the quasi-static regime (3.0 kHz MAS) improves dramatically as we move down the series, from the least (WHH-4) to the most (BR-24) compensated sequence, in a "textbook" manner. However, the performance of all three sequences degrades as the spinning speed is increased. This degradation is most marked for BR-24, again in a "textbook" manner, since the cycle time of BR-24 is significantly longer than for WHH-4 or MREV-8 (Fig. 4) leading to the prediction that it is naturally more susceptible to the time-dependence introduced by faster MAS.

We note that BR-24 performs as well as *any* of the other sequences in the 3.0 kHz regime, including the "second-generation" phase-modulated schemes.

When we look at the four phase-modulated schemes PMLG, DUMBO-1, eDUMBO-1$_{22}$, and LG4 we first see that again they all give very significantly better performance than the original LG scheme. Within this group of four sequences, we see that PMLG performs slightly less well than the other three sequences. This is expected since it has been shown that both the DUMBO sequences and (by design) LG4 can be seen as iterated versions of PMLG [20,21,41]. Indeed, the LG4 cycle is composed of two successive PMLG rotations around different angles in the xy plane. Thus, the relation between PMLG and LG4 is similar (but not the same) to the relation between WHH-4 and MREV-8. Comparing DUMBO-1, eDUMBO-1$_{22}$ and LG4 we see that DUMBO-1 tends to yield the best performance of the three at slow spinning (3.0 kHz), which is not surprising since it was developed in the static limit, while eDUMBO-1$_{22}$ tends to yield the best performance at faster rates (12.5 and 22.0 kHz), and that LG4 tends to yield good performance across the range of spinning speeds.

For alanine (Fig. 5) this results in the best linewidths at 3.0 kHz being (from BR-24) 115, 180 and 1530 Hz for CH$_3$, CH and NH$_3$ respectively. At 12.5 kHz we obtain 104, 150 and 878 Hz with eDUMBO-1$_{22}$. At 22.0 kHz we observe the best results again with eDUMBO-1$_{22}$, with linewidths of 113, 117 and 399 Hz. Note that the significant broadening of the NH$_3^+$

resonance is attributed to interference between the decoupling sequence and the molecular dynamics of the NH$_3^+$ moiety (rotation around the C—N bond).

For glycine (Fig. 6) we obtain the best results at 3.0 kHz with BR-24 and DUMBO-1. The former yields linewidths of 176, 210 and 241 Hz for CH$_{2a}$, CH$_{2b}$ and NH$_3$ respectively, while the latter yields 172, 211 and 315 Hz. At 12.5 kHz we obtain 189, 191 and 282 Hz with DUMBO-1, and at 22.0 kHz 180, 204 and 325 Hz with eDUMBO-1$_{22}$.

For β-AspAla (Fig. 7) the best results at 3.0 kHz MAS are again obtained with BR-24, which provides all linewidths narrower than 220 Hz (with the CH$_3$ linewidth of 125 Hz being the narrowest). At 12.5 kHz we observe the narrowest linewidths using DUMBO-1 and eDUMBO-1$_{22}$, which give very similar results and yield 119 Hz for the CH$_3$ linewidth. At 22.0 kHz MAS we observe again the best results using eDUMBO-1$_{22}$, which yields a linewidth of 109 Hz for the CH$_3$ group.

In order to further understand the residual broadening under homonuclear decoupling, Figs. 8–10 show the ^{1}H T_2' dephasing curves [32] measured using a double spin echo sequence [51] for alanine, glycine and β-AspAla. The T_2' values extracted by fitting these curves are given in Table S15. Transverse dephasing times are important both to further probe the mechanisms of decoupling, but also to measure the coherence lifetimes that are directly limiting for the efficiency of many correlation experiments such as J-based HSQC type experiments [56].

Analogously to the decoupled spectra in the previous figures, we see that the shortest dephasing times under all conditions and across all three samples are obtained with the basic LG (for the first generation) and PMLG (for the second generation) sequences. For the "first-generation" sequences we also see a "textbook" increase in T_2' as we go from LG to WHH-4 to MREV-8 to BR-24 (see Fig. 10a!) at the two lower spinning speeds. Interestingly, at 22.0 kHz, all four sequences yield essentially the same T_2' value. The T_2' value consistently decreases for all these sequences as we move to faster spinning speeds, in line with expectations.

For alanine, at 3.0 kHz, the longest measured T_2' for the CH$_3$ group is 11.2 ms obtained decoupling with BR-24. Note that this a factor ten longer than the shortest measured value of ~1.4 ms with both eDUMBO-1$_{22}$ and PMLG.
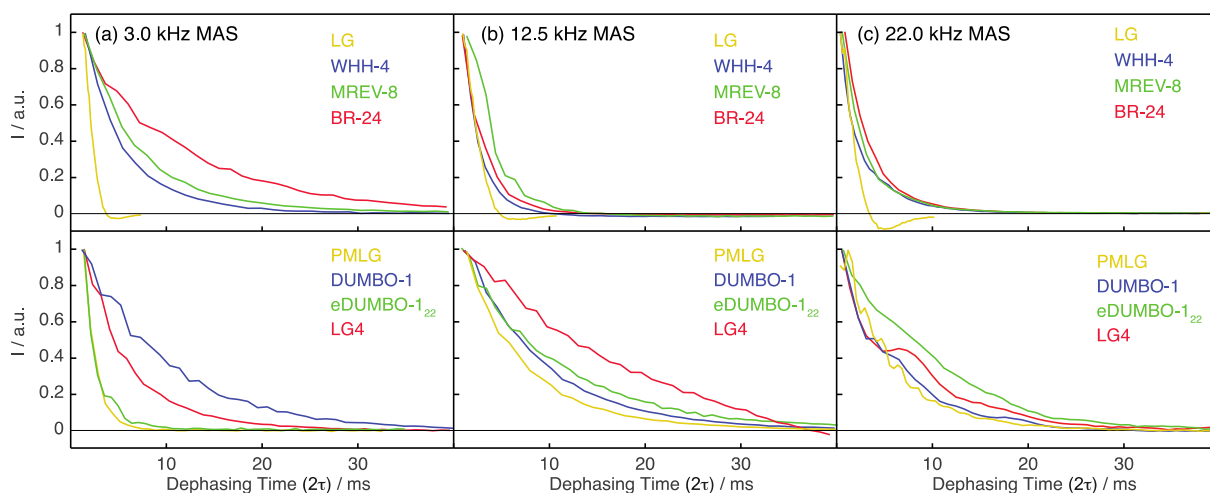
Fig. 8. Dephasing curves for CH$_3$ resonance of alanine recorded using the pulse sequence of Fig. 3c. The spectra were acquired using a MAS rate of 3.0 (a), 12.5 (b) and 22.0 (c) kHz. For decoupling we used: (top) LG (yellow), WHH-4 (blue), MREV-8 (green) and BR-24 (red), (bottom) PMLG (yellow), DUMBO-1 (blue), eDUMBO-1$_{22}$ (green) and LG4 (red). Full details on the experimental parameters are given in ESI. (For interpretation of the references to colour in this figure legend, the reader is referred to the web version of this article.)
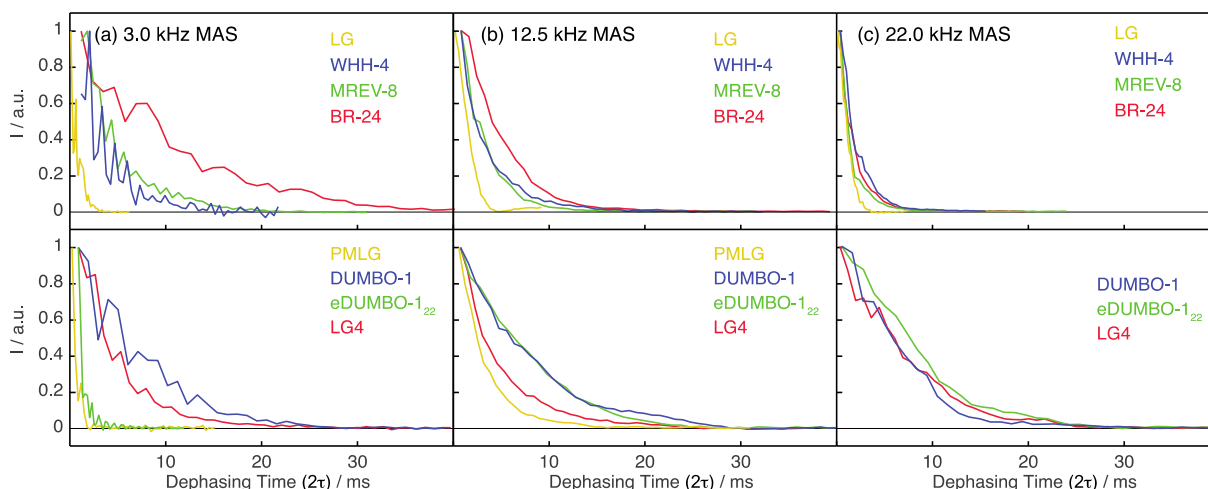
Fig. 9. Dephasing curves for CH_2 resonances of glycine recorded using the pulse sequence of Fig. 3c. The spectra were acquired using a MAS rate of 3.0 (a), 12.5 (b) and 22.0 (c) kHz. For decoupling we used: (top) LG (yellow), WHH-4 (blue), MREV-8 (green) and BR-24 (red), (bottom) PMLG (yellow), DUMBO-1 (blue), eDUMBO-1_{22} (green) and LG4 (red). Full details on the experimental parameters are given in ESI. (For interpretation of the references to colour in this figure legend, the reader is referred to the web version of this article.)
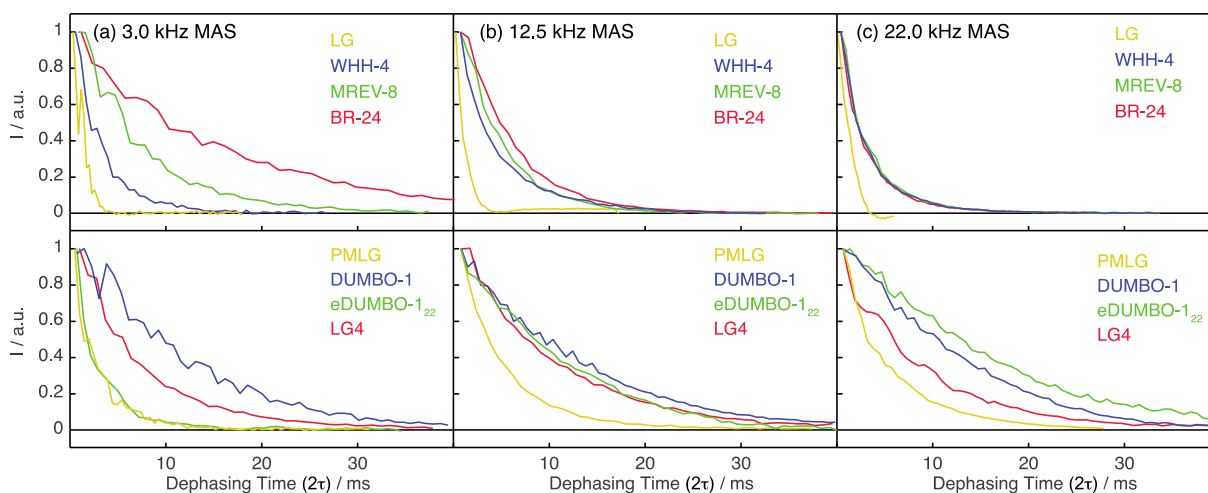
Fig. 10. Dephasing curves for CH_3 resonance of β-AspAla recorded using the pulse sequence of Fig. 3c. The spectra were acquired using a MAS rate of 3.0 (a), 12.5 (b) and 22.0 (c) kHz. For decoupling we used: (top) LG (yellow), WHH-4 (blue), MREV-8 (green) and BR-24 (red), (bottom) PMLG (yellow), DUMBO-1 (blue), eDUMBO-1_{22} (green) and LG4 (red). Full details on the experimental parameters are given in ES. (For interpretation of the references to colour in this figure legend, the reader is referred to the web version of this article.)

Interestingly, LG4 at 12.5 kHz MAS yields a T_2 of 13.4 ms, which is the longest we have observed for the CH_3 protons of alanine. This, however, is not directly reflected in the spectral resolution as this resonance is more than 60 Hz broader than in the 12.5 kHz MAS eDUMBO-1_{22} spectrum. At 22.0 kHz, the longest T_2 values are from eDUMBO-1_{22} and LG4 (9.7 and 8.4 ms respectively), while the shortest are from the windowed schemes, which all have T_2 values around 2.5 ms.

Similar T_2 results are obtained for glycine and β-AspAla with the same trends. The longest T_2 measured here is 15.3 ms for BR-24 at 3.0 kHz (corresponding to a refocused linewidth of 21 Hz), 13.4 ms for LG4 at 12.5 kHz (24 Hz), and 14.9 ms with eDUMBO-1_{22} at 22.0 kHz (21 Hz).

By combining the analysis of the spectral resolution and the T_2 values from the three compounds under analysis, we conclude that the best performing sequences in our hands in terms of decoupling performance are BR-24 and DUMBO-1 at 3.0 kHz MAS, and eDUMBO-1_{22} at 12.5 and 22.0 kHz MAS, which give both the best

spectral resolution and the longest T_2. The better performances of eDUMBO-1_{22} over the other sequences might be likely attributed to the way this sequence was developed. Indeed, being optimized directly on experimental results, the sequence might compensate for effects due to pulse imperfections (such as phase transients) and the insertion of the acquisition window. On the other side, we have systematically obtained worse results using eDUMBO-1_{22} and PMLG at 3.0 kHz MAS, and MREV-8 and BR-24 at 12.5 kHz and, especially, at 22.0 kHz MAS, where they led to very poor resolution and short T_2. LG4 never yields the absolute best performance, but it is close to optimum across the whole range of spinning speeds and samples.

While in general these results are in line with expectations, the excellent performance of BR-24 at low spinning speeds on modern consoles, in direct comparison with the second-generation sequences considered here, was unexpected by us.

As mentioned above, we note some inconsistencies between the spectral resolution and the measured T_2 values. Indeed, some of the

sequences we tested, such as PMLG, provide fairly good spectral resolution but comparatively short T_2, while others, such as LG4, led to poorer resolution than sequences yielding shorter T_2. These inconsistencies might be due to the fact that for windowless schemes we have omitted the acquisition windows when performing the indirect T_2 measurements, where these windows do directly have an effect on the resolution of 1D CRAMPS spectra. Also, when comparing T_2 values and spectral resolution we tend to assume that the residual broadening is mainly caused by residual homonuclear dipolar coupling (which is measured by the T_2). However, this is not necessarily the case, especially in the low-to-moderate regime of MAS. Indeed, it has been shown that also at the highest spinning rate available today (111.0 kHz MAS) the interactions refocused by a π pulse (the chemical shift distributions) contribute significantly to the line broadening [53,57]. If some of the sequences averages partially also some of the residual interactions that are refocused by the π pulse, then the correlation between T_2 and spectral resolution is not straightforward. Despite being a fascinating topic, the further analysis of the relation between T_2 and spectral resolution goes far beyond the scope of this manuscript.

Another important feature of homonuclear dipolar decoupling sequences is the chemical shift scaling factor. Overall, the experimental scaling factors measured here are in agreement with the expected values (details in the ESI). More interesting than the absolute value of the average scaling factor is, instead, the homogeneity of the scaling factor across the spectra. When applying homonuclear dipolar decoupling sequences, indeed, the scaling factor is rarely perfectly homogeneous among the whole spectra

[21,26,50,58–60]. As a result, the isotropic chemical shifts of the resonances we observe with CRAMPS differ slightly from the isotropic chemical shifts we obtain using MAS. Fig. 11 shows the isotropic chemical shifts values extracted from the ^{1}H CRAMPS spectra (red dots) compared to the expected values, obtained by decoupling with MAS only (grey dotted lines). The overall RMSE between all observed and expected positions is 0.15 ppm. This is certainly not negligible, and might also be underestimated due to the fact that two out of the three compounds under analysis contain only three resonances. Indeed, if we consider only β-AspAla the RMSE goes up to 0.17 ppm.

At 3.0 kHz MAS, the least good agreement between observed and expected shifts is given by PMLG, with an average RMSE for the three compounds of 0.12 ppm, while the best agreement is provided by LG4 and MREV-8, with average RMSEs of 0.02 ppm and 0.03 ppm respectively. At 12.5 kHz, the poorest agreement is given by DUMBO-1 (average RMSE of 0.12 ppm) while the best match between expected and observed shifts is obtained with LG4, with an average RMSE of 0.05 ppm. At 22.0 kHz MAS, the most accurate decoupling sequence is PMLG with an average RMSE of 0.06 ppm, while the worst results are obtained with BR-24 and DUMBO-1 (average RMSEs of 0.18 and 0.13 ppm respectively).

If we consider all spectra across the three spinning rates, LG4 clearly emerges as the most robust, with the most homogeneous scaling factor (the average RMSE is 0.05 ppm, and it never exceeded 0.12 ppm in any of the spectra) while the most inhomogeneous scaling factors are from DUMBO-1 and BR-24 (average RMSEs of 0.12 and 0.11 ppm).
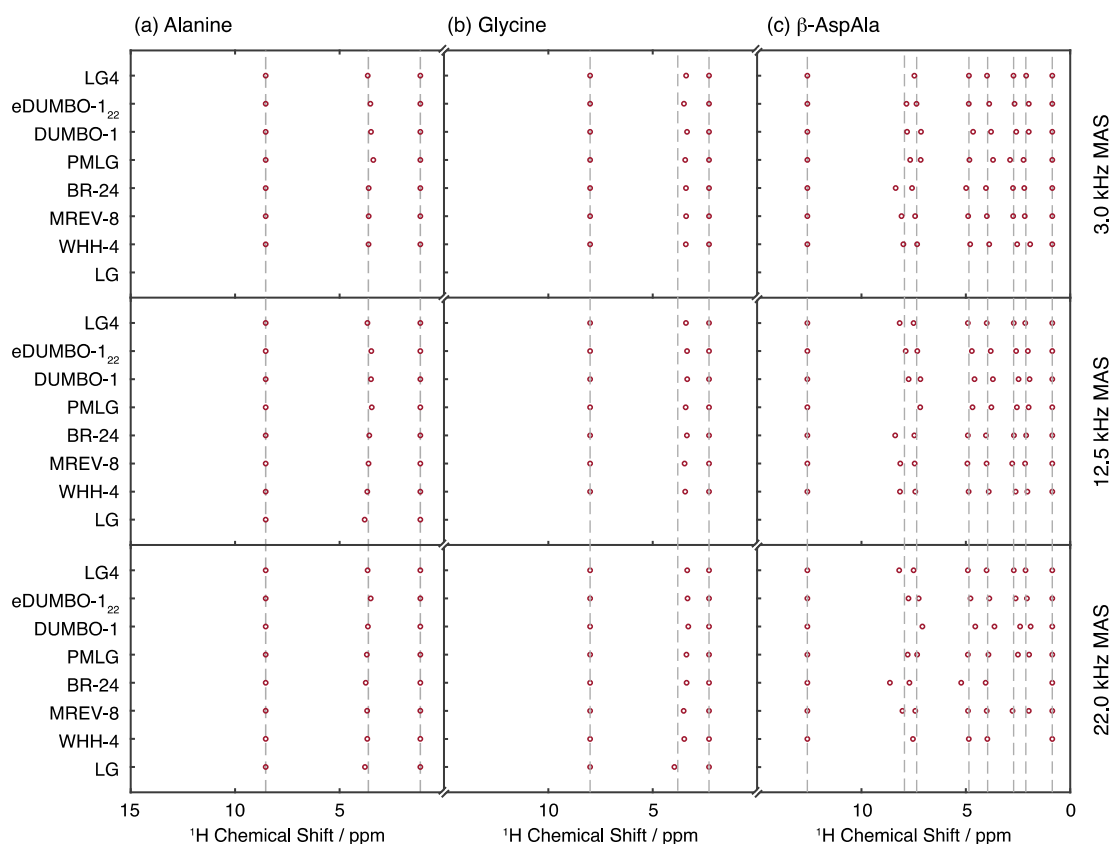
Fig. 11. Isotropic chemical shifts observed in the ^{1}H CRAMPS spectra of powdered alanine (a), powdered glycine (b) and β-AspAla (c). The spectra were acquired using a MAS rate of 3.0 (top row), 12.5 (middle row) and 22.0 (bottom row) kHz. The observed isotropic chemical shifts are shown as red dots, while the expected isotropic chemical shifts (obtained with MAS only) are shown as grey dashed lines. The missing points are chemical shifts that could not be resolved due to low resolution of the CRAMPS spectra. All observed chemical shift values are given in ESI. (For interpretation of the references to colour in this figure legend, the reader is referred to the web version of this article.)

4. Pulse sequence optimization

Fig. 12 shows the procedure we used to set up the 1D ^{1}H CRAMPS experiments shown in Section 3. We divide the setup of CRAMPS experiments into two main phases: the preparatory steps (in red in Fig. 12), which consist in a set of guidelines to consider before starting the optimization of the pulse scheme, and the optimization steps (in yellow in Fig. 12), where the experimental parameters are tuned in order to provide the best possible decoupling. Note that this second phase it is not exactly the same for all pulse schemes, as some of them may have extra parameters to consider. We will group the optimization step into two categories: windowed (WHH-4, MREV-8 and BR-24) and windowless (LG, PMLG, DUMBO-1, eDUMBO-1$_{22}$ and LG4) schemes. Despite some small technical differences, the guidelines for the optimization are general and can be extended to other homonuclear dipolar decoupling schemes not investigated here.
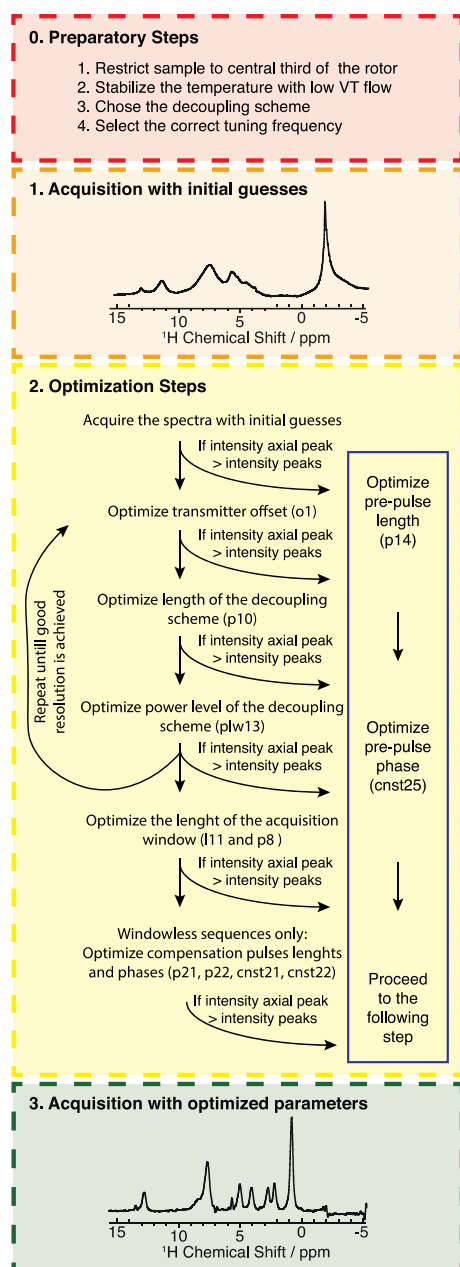

Fig. 12. Schematic representation of the procedure to setup CRAMPS experiments described in Section 4 and Appendix A.

The step by step protocol is described in detail in Appendix A, while the "au" program and pulse sequences necessary to implement these experiments are given in ESI. Note that there are a few other examples of guidelines to set up homonuclear dipolar decoupling experiments in the literature [21,27,46,61,62]. Despite being more focused on specific decoupling schemes, we strongly encourage the reader to consult them to complement the material reported here.

Fig. 13 shows the effect of several experimental parameters on CRAMPS spectra. Fig. 13a and b show that the spectral resolution it is not only affected by the parameters of the pulse scheme, but also by other experimental variables such as the confinement of the sample to a restricted volume of the rotor, or the probe tuning frequency, which are taken into account in the "preparatory phase" (see Appendix A.1). However, the quality of a CRAMPS spectrum is mostly affected by the parameters of the pulse scheme (Fig. 13c–n), which are tuned in the "optimization phase" (see Appendix A.2).

The overall quality of a CRAMPS spectrum depends on three factors: the spectral resolution, the intensity of the axial peak, and the presence of artefacts [46]. Ideally, the resolution should be as high as possible, while the axial peak and the artefacts should be absent. To generalize, the spectral resolution is mostly affected by the transmitter offset (Fig. 13c), the cycle time (τ_c) (Fig. 13f and g), the length of the acquisition window (τ_{acq} - for windowless sequences only) (Fig. 13i and j) and the decoupling power level (Fig. 13h). The intensity of the axial peak is mostly affected by the overall phase angle and the phases and lengths of the prepulse (the pulse θ after the initial $\pi/2$) (Fig. 13d and e) and compensation pulses θ_{c1} and θ_{c2} (when present) (Fig. 13k–n). Note that this separation between parameters that influence resolution and the axial peak is indicative, as there can be significant cross talk. Finally, the intensity of the artefacts can be adjusted by changing the length of the acquisition window, and their position by moving the transmitter offset. However, to obtain spectra completely free of artefacts is not trivial, and it is often achieved in conditions which do not maximize the spectral resolution. As a consequence, it is usually better to adjust the transmitter position so that the artefacts are far from the peaks of interest.

Note that the intensity of the axial peak and the number of artefacts can be lowered (often suppressed) also through the implementation of supercycled sequences [49,50]. Supercycling here means to apply a phase increment of $2\pi/n$ (where n is usually equal to 2) between consecutive decoupling elements. This leads to the generation of an effective field along the z axis, which can produce cleaner spectra, with fewer (and smaller) artefacts and lower intensity of the axial peak without further optimization. However, this also produces a significant reduction of the scaling factor, and therefore resolution, which is a major drawback of such an implementation. As a consequence, we recommend using sequences that are not supercycled, and where the optimization process described here provides spectra which are equally clean.

5. Conclusions

In summary, we compared the experimental performances of ^{1}H CRAMPS experiments using eight homonuclear dipolar decoupling sequences (LG, WHH-4, MREV-8, BR-24, PMLG, DUMBO-1, eDUMBO-1$_{22}$ and LG4) on three different powdered samples (alanine, glycine and β-AspAla) and at three different MAS rates (3.0, 12.5 and 22.0 kHz). We compare these sequences by analysing spectral resolution, T_2 values and homogeneity of the scaling factors. We show that the best spectral resolution and the longest T_2 values are given by BR-24 and DUMBO-1 at 3.0 kHz MAS, and eDUMBO-1$_{22}$ at 12.5 and 22.0 kHz MAS. LG4 never yields the
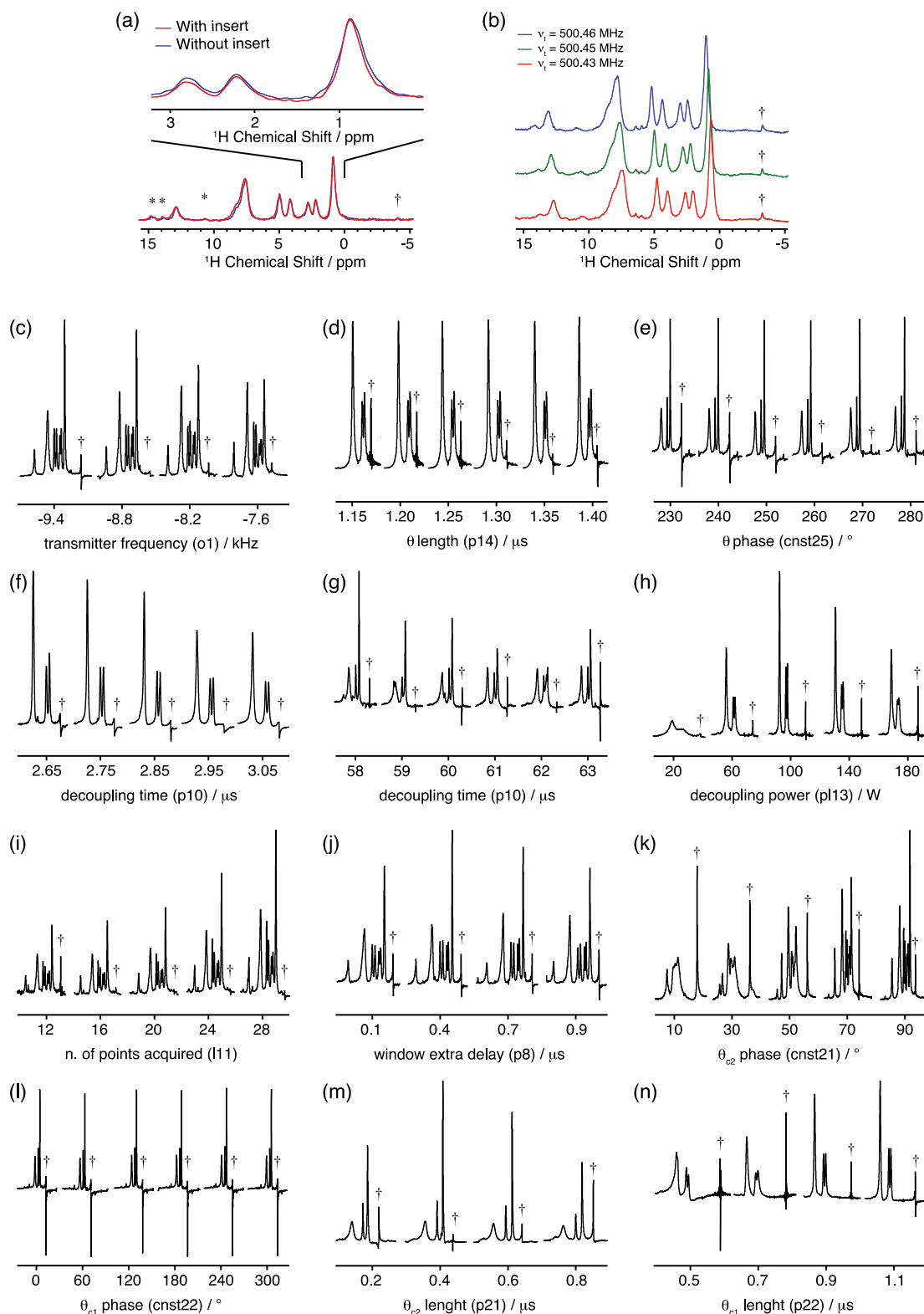
Fig. 13. Optimization of ^{1}H CRAMPS experiments. (a) Spectra acquired with (red) and without (blue) a Teflon insert. (b) Spectra acquired with different tuning frequencies (ν_t). (c–p) Examples of decoupling performance as a function of (c) transmitter offset, (d) pre-pulse length, (e) pre-pulse phase, (f–g) length of the decoupling element for windowed (f) and windowless (g) schemes, (h) power level of the decoupling element, (i) number of FID points acquired during each acquisition window, (j) extra delay in the acquisition window, (k–l) phase of the compensation pulses θ_{c2} (k) and θ_{c1} (l), (m–n) length of the compensation pulses θ_{c2} (m) and θ_{c1} (n). Spectra (a–c, i–k) were acquired using β-AspAla, (d, f, h and n) using glycine and (e, g, l and m) using alanine. The decoupling scheme was eDUMBO-1$_{22}$ in (a, b, g, j and m), LG4 in (c, i and k), WHH-4 in (d), BR-24 in (f) and PMLG in (e, h and l). MAS rates were 22.0 kHz in (a, b, e, g, j, k and l), 12.5 kHz in (c, d, h, m and n) and 3.0 kHz in (f and i). (For interpretation of the references to colour in this figure legend, the reader is referred to the web version of this article.)

absolute best performance, but it is close to optimum across the whole range of spinning speeds and samples and is the sequence that gives the most homogeneous scaling factor (with an average RMSE between chemical shifts observed with LG4 CRAMPS and with MAS experiments of 0.05 ppm). Finally, we have provided a detailed set of guidelines to optimise the performances of ^{1}H CRAMPS experiments, together with all the pulse and "au" programs necessary to run these experiments.

Declaration of Competing Interest

There are no conflicts to declare.

Acknowledgments

Appendix A

In the following, we provide guidelines for setting up and optimizing 1D ^{1}H CRAMPS experiments. We describe the step by step protocol used to acquire the data shown in Section 3, and we provide in the ESI all the necessary pulse sequences and "au" programs to implement these sequences. Note that, while the pulse and "au" programs were written for a Bruker Avance III HD console with Topspin 3.5, and might require modifications if used on a different system, the guidelines for the optimization are general and can be extended to other homonuclear dipolar decoupling schemes which were not investigated in this work. As mentioned in Section 4, there are a few other examples of guidelines to set up homonuclear dipolar decoupling experiments in the literature [21,27,46,61,62]. Despite being more focused on specific decoupling schemes, we strongly encourage the reader to use them to complement the material reported here. In particular, Ref. [61] offers a comprehensive study of experimental aspects for the optimization of LG-based decoupling schemes, and compared to our work it provides additional details on the effects of several experimental parameters on the scaling factor, and studies the dependence of the spectral resolution from relevant spectrometer default timings, such as the transmitter blanking time (*BLKTR*) and the phase presetting time (*PHASPR*).

A.1. Preparatory steps

Good practice for the acquisition of CRAMPS spectra starts when packing the sample. At this stage while this may depend on individual probes, we systematically restrict the sample to the central third of the rotor with the thought that this will reduce sensitivity to *rf* inhomogeneity. Restricting the sample will not always make a large difference [61], but it is never detrimental in our hands. Using inserts with spherical samples has been suggested in the past [63,64], but in our hands this has always proven to be very difficult to implement and has not led to observably better performance than simple restriction to the central third, which is what we thus recommend here. Fig. 13a shows an example of the gain in resolution obtained by confining the sample, in the case of a spectrum of β-AspAla acquired using eDUMBO-1$_{22}$. Here, the linewidth of the methyl resonance (at 0.86 ppm) decreases from 185.7 Hz (blue spectra) to 160.3 Hz (red spectra) when adding the Teflon insert, which corresponds to about a 14% gain in resolution.

Once the sample is packed and inserted into the probe, it is important to always actively control the sample temperature with the variable temperature (VT) gas. Indeed, changes in temperature can lead to small changes in probe tuning, that will change decou-

pling performance. Additionally, the application of high power *rf* pulses leads to additional heating, that can also lead to extra line broadening contributions. The application of active temperature control limits these effects. However, note that using overly high VT flows sometimes leads to micro vibrations of the rotor (visible on the probe tuning wobble curve) which can also affect the quality of the spectra by increasing the quantity and intensity of the artefacts. (All our experiments were done using a VT flow of 600 l/h).

The next step is the selection of the decoupling scheme, in the light of the guidelines given in Section 3 depending on the MAS rate desired. Note that at higher spinning rates than 22.0 kHz, sequences such as PMLG, DUMBO-1 and eDUMBO-1$_{22}$ have been shown to still provide good resolution [9–11] (and presumably LG4), but the best decoupling performances at 65.0 kHz MAS were so far obtained with sequences specifically developed to work in the very-fast spinning regime such as eDUMBO-PLUS-1 [11] or TIMES/TIMES$_0$ [12,13].

The next parameter to consider is the probe tuning frequency (v_t). Fig. 13b shows three spectra of β-AspAla acquired by detuning the probe from 500.43 MHz (the transmitter offset) to 500.46 MHz. We note the strong effect of the tuning frequency on the peak positions, which are significantly shifted to higher frequencies when v_t increases. This frequency shift has been explained by Vega in terms of phase transients [59]. Note that changes of v_t also affect the spectral resolution. In the spectra of Fig. 13b the linewidth of the methyl resonance goes from 202 Hz in the spectra acquired using v_t of 500.43 and 500.46 MHz, to 182 Hz using v_t of 500.45 MHz; about a 10% gain in resolution. To begin, the probe should be tuned at the frequency at which the probe gives the minimum reflected power (as shown by the probe tuning wobble curve). The tuning can then be adjusted toward the end of the optimization to find the v_t value that gives the highest resolution.

The spectrometer pulse program to use will be different depending on the choice of the decoupling scheme. Windowless decoupling schemes (LG, PMLG, DUMBO-1, eDUMBO-1$_{22}$ and LG4 – Fig. 4a, e–h) require the use of a pulse program corresponding to Fig. 3a, where an acquisition window is added between decoupling pulses in order to periodically sample the FID and pulse are implemented directly using quadrature phases. The second-generation decoupling schemes are all implemented as continuous phase-modulated pulses (as is LG), which can be generated using the "au" programs provided in ESI. The parameters to select when generating a shaped pulse are: (i) the number of phase steps, (ii) the number of decoupling cycles to repeat between each acquisition window and (iii) the offset. The number of phase steps depends on the pulse resolution of the console in use. The Avance III HD system has a resolution of 0.1 μs, so a pulse of 10 μs can be described using up to 100 steps. We found that the number of phase steps used to describe the sequence does not have a significant influence on the resolution, unless too few. Here we used 64 steps to describe each cycle of DUMBO-1, eDUMBO-1$_{22}$, LG and PMLG (despite the latter is usually implemented using only 6, 10 or 18 steps each cycle – respectively dubbed as wPMLG3, wPMLG5 and wPMLG9 [47,65]) and 120 steps to describe LG4. The number of decoupling cycles between each acquisition window should be optimized. We found that the best resolution was achieved with 2 cycles for DUMBO-1 and eDUMBO-1$_{22}$, 3 cycles for LG4 and 1 cycle for LG and PMLG. In the following, we will use the term "decoupling element" to refer to the group of decoupling cycles applied between two consecutive acquisition windows. The last parameter to choose during the generation of the shaped pulse is the starting phase, which changes the direction of the effective field in the xy plane by incrementing the phase of the whole waveform. In the next section, we will describe in detail how to perform the optimization of this phase.

Windowed schemes (WHH-4, MREV-8 and BR-24 - Fig. 4b–d) require the pulse scheme of Fig. 3b, where the FID is sampled in acquisition windows placed within the decoupling cycle. Note that the presence of an intrinsic acquisition window within the decoupling scheme is an advantage for homonuclear decoupling, since, adding a delay for acquisition may degrade performance. We use one acquisition window per cycle, centered in the first 2τ delay. Note that to maximize the signal to noise ratio it is possible to use multiple acquisition windows per decoupling cycle if a proper post-acquisition FID reconstruction is performed [36]. The overall phase again plays an important role also for these sequences, and needs to be adjusted to obtain the correct orientation of the effective field. Since these schemes do not require the generation of a shaped pulse, this is done using the constant *cnst10* in the pulse program, which adds to the phase of all the $\pi/2$ pulses. Further details on the optimization of this phase can be found in the next section.

A.2. Optimization steps

The optimization then starts with the acquisition of a spectrum using guess parameters (for example, which were previously optimized for another system, or alternatively using the set of initial parameters we give in ESI) as a starting point. Note that before acquiring the first spectrum it is important for the safety of the probe to adjust the acquisition time. Due to the application of high power *rf* pulses between acquisition windows, the acquisition time should be kept as short as possible for the sample under analysis. In our experiments, we never exceed 35 ms acquisition times, and we typically use about 20 ms. This limitation is not only related to the duty cycle of the probe itself, but also to the fact that the longer the application of high power *rf* pulses, the higher the chance to significantly heat up the sample, introducing extra line broadening effects.

A.2.1. Transmitter frequency

After the acquisition of the initial spectrum, the optimization of the pulse program parameters should begin with a rough adjustment of the transmitter offset (*o1* in the pulse program, in steps of 500 Hz). As shown in Fig. 13c, the position of the transmitter offset affects both the spectral resolution and the intensity of the axial peak. The aim of this first step is to avoid overlap with any of the resonances of interest, as the transmitter frequency and the zone nearby will appear distorted in the spectrum. In terms of resolution, best results are usually obtained when the transmitter is positioned on the right hand side of the spectrum, as close as possible to the peaks of interest but far enough to avoid distortion of the zone of interest [46,59]. While optimizing the transmitter frequency, it is also important to ensure that the positions of the artefacts do not overlap with the peaks. The position of the transmitter offset will then be refined in the following steps.

A.2.2. Suppression of the axial peak

During the optimization of the transmitter offset, as well as of other parameters that influence the intensity of the axial peak, the axial peak might likely become so intense to overwhelm the spectra itself. In such a case, the adjustment of the pre-pulse length and the overall phase angle became necessary to continue with the optimization. One way to experimentally determine the values of these two parameters was originally introduced by Lesage and co-workers [46]. Despite being a very precise method to determine both pre-pulse length and offset angle, able in most cases to completely suppress the axial peak, this method has also some disadvantages. In particular, it (i) requires the use of a different pulse program than the one used for the direct acquisition of ^{1}H CRAMPS spectra, (ii) requires the generation of multiple phase-modulated

waveforms when windowless schemes are used and (iii) assumes continuous decoupling without considering the effect of the acquisition window. As a result, the process is time consuming and used as a last resort. The direct optimization of the pre-pulse phase (*cnst25* in the pulse program) is a faster way to suppress the axial peak in 1D ^{1}H spectra, and usually provides satisfactory results. This optimization can be run directly in the 1D spectra, in concert with the optimization of the pre-pulse length (*p14* in the pulse program) to quickly remove the axial peak (Fig. 13d–e). In the initial stages of optimization, where there is no need of completely suppress the axial peak, the phase can be optimized in steps of 20/30° (from 0° to 360°) and the length in steps of 0.2/0.25 μs (from 0 to 1.5 μs). The step sizes should then be decreased later on in the optimization, when approaching the final result. These two parameters should be refined whenever the intensity of the axial peak is higher than the most intense peak in the spectra.

A.2.3. Length and power level of decoupling element

The following two parameters to optimize are the length and the power level of the decoupling element, which both play a central role in the maximization of the spectral resolution. The optimization protocol is slightly different for windowed and windowless schemes.

Windowed Schemes. In windowed schemes, the length of the decoupling cycle is defined by the delay τ shown in Fig. 4b–d (*p10* in the pulse programs). The minimum value of τ is limited by the length of the acquisition window, which is positioned within a 2τ delay in the decoupling cycle, and by the length of the $\pi/2$ pulses, which must be subtracted from the τ and 2τ delays to maintain the symmetry typical of windowed sequences. A good strategy to find the optimal length of decoupling cycle is to start setting up τ as small as possible, and then to increment it of 2 to 3 μs in steps of 0.05 to 0.1 μs. For the windowed decoupling schemes we test in this work, we found that shorter decoupling cycles provide better resolution, as shown in Fig. 13f. We usually set τ to 0.05 or 0.1 μs larger than the minimum possible value, as the spectral resolution remains almost unchanged, but the intensity of the artefacts decreases. For optimal resolution, the power level for these sequences (*pl13* in the pulse program) should be set as high as the duty cycle of the probe allows, due to the fact that the length of the $\pi/2$ pulses limits the length of the decoupling cycle. Besides the effect on the cycle length, we do not observe any significant direct influence of the power level on the spectral resolution (keeping τ constant) with the *rf* amplitudes used here. Note that the calibration of the $\pi/2$ pulse is very important to maximize the performance of these sequences, as miscalibrated pulses provide poorer resolution and lower scaling factors. Once both the length and the power level of the decoupling cycle are set, the transmitter offset should be tuned (in steps of 100/200 Hz) to obtain optimal resolution. For windowed sequences, we found that the transmitter position is relatively independent of the length of the decoupling cycle.

Windowless Schemes. Windowless schemes require a more careful optimization of length and power level of the decoupling element. The spectral resolution is strongly influenced by the interplay of these two parameters and the transmitter offset, and a missetting of one of these values can dramatically decrease the quality of the spectra. From our experience, the most efficient way to find optimal values for these three parameters is through an iterative optimization of each of them while keeping the other two fixed.

We usually start by adjusting the length of the decoupling element (*p10* in the pulse program) while keeping the power level constant (Fig. 13g). At the beginning of the optimization this parameter can be screened from the smallest possible pulse length (which depends on the number of steps used to describe the shaped pulse) up to a few tens of μs, in large steps of about 5 μs

(depending on the decoupling scheme used and the number of decoupling cycles repeated, the length of the decoupling element might also exceed 100 µs). The range of decoupling lengths that provide better resolution in this first screening should be further investigated using smaller steps (down to 1–2 µs). Note that the optimal decoupling time strongly depends on the rotor period (τ_r). In particular, strong recoupling conditions which lead to very poor resolution are observed when the decoupling cycle time and the rotor period are synchronized ($\tau_c/\tau_r = n/2$, where n is an integer) [46,65,66]. While the conditions where recoupling occurs are clear and can be calculated, there conversely is not a known relation of cycle time and rotor period that guarantee good resolution. As a guideline, in our experiments we often observed optimal resolution with τ_c/τ_r around 0.2, 0.7 and 1.2 for windowless homonuclear dipolar decoupling schemes. These are however purely empirical observations and do not guarantee optimal resolution.

Once the length of the decoupling element is set to a value that provides good spectral resolution, the decoupling power level (*pl13* in the pulse program) is adjusted. An example of the optimization of this parameter is shown in Fig. 13h. Initially, we suggest screening the decoupling power from low power levels (few Watts) up to the maximum value allowed by the duty cycle in steps of 10/20 W. Then, the region of power levels that provides best decoupling should be further investigated using smaller step sizes (around 5 W).

Following the optimization of length and power level of the decoupling element, the transmitter frequency should be readjusted with a smaller step size as compared to the initial optimization (around 100/200 Hz).

To find optimal resolution, the optimization of these three parameters should be iteratively repeated decreasing gradually both the screening window and the step size (down to about 0.25 µs, 2 W and 100 Hz for the length and power level of the decoupling element and transmitter frequency respectively). Note that to reach a satisfying spectral resolution might require several iterative loops, especially when the starting point is far from the optimal conditions. Note also that the combination of decoupling length and power level affects the scaling factor of the sequence, which should be taken into account while finding the optimal values.

A.2.4. Acquisition window

The next step is the optimization of the acquisition window. On an Avance III spectrometer, the acquisition window is composed by an initial receiver deadtime of 1.6 µs, a delay of variable length to turn the receiver on and sample n complex points, 0.1 µs to turn off the receiver, and an extra variable delay. The two parameters to tune are: the number of complex points to acquire during each acquisition window (*l11* in the pulse program) and (for windowless sequences only) the delay that follows the receiver closure (*p8* in the pulse program).

Windowed Schemes. In windowed schemes the acquisition window is inserted within the decoupling cycle, limiting its minimum duration. It plays a critical role in spectral resolution, which we found to be remarkably better with shorter cycle lengths (see Section A.2.3). As a consequence, the acquisition window should be as short as possible. We obtained optimal resolution acquiring 3 complex points per decoupling cycle (*l11* = 6). Note that currently for windowed sequences the delay after receiver closure it is not a tuneable parameter. It has a fixed value of 1.4 µs, and it is used to centre the acquisition window in the 2τ delay of the decoupling scheme (this delay is encoded in the pulse program and is not under the control of the user).

Windowless Schemes. In windowless sequences the acquisition window is positioned between two decoupling elements, giving a higher degree of freedom for its optimization compared to windowed schemes. However also for these sequences the acquisition windows should be kept short due to the absence of homonuclear dipolar decoupling, which leads to broad spectra when long windows are used.

Fig. 13l shows an example of the optimization of the number of complex points acquired after each decoupling cycle. Increasing this value increases the spectral sensitivity, and at the same time affects slightly both the spectral resolution and the scaling factor. Since for organic solids the ^1H sensitivity is usually not a limiting problem, we selected the correct values based solely on the resolution, which is given by the combination of linewidth and scaling factor. For most schemes, we found optimal resolution using *l11* equal to 16 (except for LG4 where the optimal value was 26, probably due to the longer decoupling element).

Fig. 13m shows an example of optimization of the delay after the closure of the receiver. To find the optimal value, we suggest screening this parameter from 0 to 1 µs in steps of 0.1 µs. In general, we found the best values for this parameter to be often lower than 0.5 µs, and that values higher than 1 µs provide systematically poorer resolution.

A.2.5. Compensation pulses

This step has to be performed for windowless sequences only, which have two compensation pulses (θ_{c1} and θ_{c2}) at the beginning and at the end of each decoupling element. These pulses were originally developed for PMLG and LG4 to remove the chemical shift scaling factor distortion that occurs near the transmitter frequency in 1D CRAMPS experiments [21]. We found that phenomenologically the addition of these two pulses improves the spectral resolution also when using the other windowed decoupling schemes tested in this work.

In their original implementation, these pulses were of the same length, always smaller than 0.5 µs. In contrast, we found that the best results are obtained when both the lengths (as well as the phases) of these two pulses are independently optimized. Typically, we start their optimization by fixing the pulse lengths to a relatively short value, about 0.3 µs, and by screening over 360° the phase of the θ_{c2} pulse in steps of 5° (this can be done by changing the constant *cnst21* in the pulse program). The value of the θ_{c2} phase affects significantly both the spectral resolution and the intensity of the axial peak, as shown in Fig. 13k. However, the choice of the optimal value for this parameter should be based solely on the spectral resolution, as the axial peak can be suppressed in a later stage by modifying the pre-pulse parameters. The optimization of the phase of the pulse θ_{c1} can be performed in a similar way (changing the constant *cnst22* in the pulse program), but from our experience we found that it has a much smoother effect on the spectral resolution compared to the θ_{c2} phase (Fig. 13l). Note that screening these phases over 360° is not necessary if, initially, the axial peak is adjusted by changing the phase of the decoupling element instead of the pre-pulse (see Section A.2.2). In this case, the correct values for the parameters *cnst21* and *cnst22* should be close to 0, and the optimization can be run in a smaller range (from −30° to +30° in steps of 5°).

Once the θ_{c1} and θ_{c2} phases are set, we focus on their lengths, whose effects on the quality of the spectra are shown in Fig. 13j and k respectively for θ_{c2} and θ_{c1}. This optimization should be performed in an iterative way, changing one pulse length at the time while keeping all other parameters constant. We start by screening the length of θ_{c2} (*p21* in the pulse program) from 0 to 1.2 µs in steps of 0.1 µs, followed by the same optimization for the θ_{c1} length (*p22* in the pulse program). Then, this procedure should be iteratively repeated decreasing the step size (down to 0.025 µs) until optimal resolution is achieved.

A.2.6. Final adjustments

At this stage, the optimization of both windowed and window-less decoupling schemes is nearly finished, and the quality of the spectra should be comparable to the ones shown in the section above. The last step is the fine tuning of the pre-pulse length and phase, in order to completely suppress the axial peak. Being the last step, these two parameters should be screened using small step sizes (0.025 μs and 2° for length and phase of the pre-pulse respectively). The tuning of these two parameters should lead to a high-resolution ^{1}H spectrum with a minimized axial peak.

A.2.7. Scaling factor correction & referencing

The axis of the acquired spectrum then needs to be corrected for the chemical shift scaling factor. This can be measured by comparing the distance between two peaks in the ^{1}H CRAMPS spectrum with the distance between the same peaks in the MAS spectrum. The correction of the spectrum can then be done at the spectrometer by dividing the acquisition spectral width by the scaling factor (using the command "s swh" in TopSpin), and Fourier transforming again. The chemical shift values extracted from the MAS spectrum should be used to calibrate on an absolute scale the chemical shift axis of the CRAMPS spectrum.

When it is not possible to resolve at least two peaks in the MAS spectrum, it is necessary to use an external reference for the calculation of the chemical shift scaling factor and for the calibration of the chemical shift axis on an absolute scale. In this case, the optimization of the CRAMPS parameters should be performed on the compound under analysis, and then the CRAMPS spectrum of the reference compound should be acquired under the exact same conditions. Note that the optimization of the CRAMPS parameters on the sample of interest is preferred, however in some cases (such as complex samples, samples with low sensitivity or long relaxation times) it is easier to carry out also the optimization on an external reference (we suggest to use one of the three standard compounds used here). Each time an external reference is used, it is important to take into account the influence of the probe tuning frequency on the observed chemical shifts, mentioned in Section A.1 and shown in Fig. 13b. To avoid inconsistent referencing, it is indeed very important to use the same value of ν_t to acquire the CRAMPS spectra of the compound under analysis and of the reference.

Appendix B. Supplementary material

Supporting data files can be found online at https://doi.org/10.17632/4k67zvw67g.1.

Supplementary information to this article can be found online at https://doi.org/10.1016/j.jmr.2019.106598.

References

[1] M. Lee, W.I. Goldburg, Nuclear-magnetic-resonance line narrowing by a rotating rf field, Phys. Rev. 140 (1965) A1261–A1271.

[2] W.I. Goldburg, M. Lee, Nuclear magnetic resonance line narrowing by a rotating rf field, Phys. Rev. Lett. 11 (1963) 255.

[3] J.S. Waugh, L.M. Huber, U. Haeberlen, Approach to high-resolution NMR in solids, Phys. Rev. Lett. 20 (1968) 180–182.

[4] U. Haeberlen, J.S. Waugh, Coherent averaging effects in magnetic resonance, Phys. Rev. 175 (1968) 453–467.

[5] E. Andrew, A. Bradbury, R. Eades, Removal of dipolar broadening of nuclear magnetic resonance spectra of solids by specimen rotation, Nature 183 (4678) (1959) 1802.

[6] I. Lowe, Free induction decays of rotating solids, Phys. Rev. Lett. 2 (1959) 285.

[7] W. Rhim, A. Pines, J. Waugh, Time-reversal experiments in dipolar-coupled spin systems, Phys. Rev. B 3 (1971) 684.

[8] B.C. Gerstein, R.G. Pembleton, R.C. Wilson, L.M. Ryan, High resolution NMR in randomly oriented solids with homonuclear dipolar broadening: combined multiple pulse NMR and magic angle spinning, J. Chem. Phys. 66 (1977) 361.

[9] M. Leskes, S. Steuernagel, D. Schneider, P.K. Madhu, S. Vega, Homonuclear dipolar decoupling at magic-angle spinning frequencies up to 65kHz in solid-state nuclear magnetic resonance, Chem. Phys. Lett. 466 (2008) 95–99.

[10] E. Salager, R.S. Stein, S. Steuernagel, A. Lesage, B. Elena, L. Emsley, Enhanced sensitivity in high-resolution ^{1}H solid-state NMR spectroscopy with DUMBO dipolar decoupling under ultra-fast MAS, Chem. Phys. Lett. 469 (2009) 336–341.

[11] E. Salager, J.-N. Dumez, R.S. Stein, S. Steuernagel, A. Lesage, B. Elena-Herrmann, L. Emsley, Homonuclear dipolar decoupling with very large scaling factors for high-resolution ultrafast magic angle spinning ^{1}H solid-state NMR spectroscopy, Chem. Phys. Lett. 498 (2010) 214–220.

[12] Z. Gan, P.K. Madhu, J.-P. Amoureux, J. Trébosc, O. Lafon, A tunable homonuclear dipolar decoupling scheme for high-resolution proton NMR of solids from slow to fast magic-angle spinning, Chem. Phys. Lett. 503 (2011) 167–170.

[13] Y. Nishiyama, X. Lu, J. Trébosc, O. Lafon, Z. Gan, P.K. Madhu, J.-P. Amoureux, Practical choice of ^{1}H–^{1}H decoupling schemes in through-bond ^{1}H–{X} HMQC experiments at ultra-fast MAS, J. Magn. Reson. 214 (2012) 151–158.

[14] P. Mansfield, Symmetrized pulse sequences in high resolution NMR in solids, J. Phys. C: Solid State Phys. 4 (1971) 1444.

[15] D.P. Burum, W.K. Rhim, Analysis of multiple pulse NMR in solids. III, J. Chem. Phys. 71 (1979) 944.

[16] M. Mehring, J. Waugh, Magic-angle NMR experiments in solids, Phys. Rev. B 5 (1972) 3459.

[17] D. Burum, M. Linder, R. Ernst, Low-power multipulse line narrowing in solid-state NMR, J. Magn. Reson. 44 (1981) (1969) 173–188.

[18] A. Bielecki, A. Kolbert, M. Levitt, Frequency-switched pulse sequences: homonuclear decoupling and dilute spin NMR in solids, Chem. Phys. Lett. 155 (1989) 341–346.

[19] E. Vinogradov, P.K. Madhu, S. Vega, High-resolution proton solid-state NMR spectroscopy by phase-modulated Lee-Goldburg experiment, Chem. Phys. Lett. 314 (1999) 443–450.

[20] M.E. Halse, L. Emsley, Improved phase-modulated homonuclear dipolar decoupling for solid-state NMR spectroscopy from symmetry considerations, J. Phys. Chem. A 117 (2013) 5280–5290.

[21] M.E. Halse, J. Schlagnitweit, L. Emsley, High-resolution ^{1}H solid-state NMR spectroscopy using windowed LG4 homonuclear dipolar decoupling, Isr. J. Chem. 54 (2014) 136–146.

[22] M. Hohwy, P. Bower, H.J. Jakobsen, N.C. Nielsen, A high-order and broadband CRAMPS experiment using z-rotational decoupling, Chem. Phys. Lett. 273 (1997) 297–303.

[23] M. Hohwy, N.C. Nielsen, Elimination of high order terms in multiple pulse nuclear magnetic resonance spectroscopy: application to homonuclear decoupling in solids, J. Chem. Phys. 106 (1997) 7571.

[24] M.H. Levitt, Symmetry in the design of NMR multiple-pulse sequences, J. Chem. Phys. 128 (2008) 052205.

[25] D. Sakellariou, A. Lesage, P. Hodgkinson, L. Emsley, Homonuclear dipolar decoupling in solid-state NMR using continuous phase modulation, Chem. Phys. Lett. 319 (2000) 253–260.

[26] B. Elena, G. de Paëpe, L. Emsley, Direct spectral optimisation of proton–proton homonuclear dipolar decoupling in solid-state NMR, Chem. Phys. Lett. 398 (2004) 532–538.

[27] P. Jackson, R.K. Harris, A practical guide to combined rotation and multiple-pulse NMR spectroscopy of solids, Magn. Reson. Chem. 26 (1988) 1003–1011.

[28] U. Haeberlen, High Resolution NMR in Solids: Advances in Magnetic Resonance, Academic Press, 1976.

[29] J. Iwamiya, S. Sinton, H. Liu, S. Glaser, G. Drobny, Multiple-pulse sequences for homonuclear decoupling. experimental verification, J. Magn. Reson. 100 (1992) (1969) 367–375.

[30] U. Haeberlen, Line Narrowing by Multiple Pulse Techniques III. Experimental Aspects, in: Nuclear magnetic resonance in solids, Springer, 1977, pp. 251–257.

[31] R. Vaughan, D. Elleman, L. Stacey, W.K. Rhim, J. Lee, A simple, low power, multiple pulse NMR spectrometer, Rev. Sci. Instrum. 43 (1972) 1356–1364.

[32] A. Lesage, M. Bardet, L. Emsley, Through-bond carbon–carbon connectivities in disordered solids by NMR, J. Am. Chem. Soc. 121 (1999) 10987–10993.

[33] B. Gerstein, High-resolution NMR in solids with strong homonuclear dipolar broadening: combined multiple-pulse decoupling and magic angle spinning, Philosoph. Trans. Royal Soc. London Series A, Mathem. Phys. Sci. 299 (1981) 521–546.

[34] M.L. Buszko, C. Bronnimann, G. Maciel, ^{1}H CRAMPS based on TREV, J. Magn. Reson., Ser A 103 (1993) 183–187.

[35] M. Levitt, A. Kolbert, A. Bielecki, D. Ruben, High-resolution ^{1}H NMR in solids with frequency-switched multiple-pulse sequences, Solid State Nucl. Magn. Reson. 2 (1993) 151–163.

[36] T.M. Barbara, L. Baltusis, Phase-cycled, multiple-window-acquisition, multiple-pulse NMR spectroscopy, J. Magn. Reson., Ser A 106 (1994) 182–187.

[37] H. Cho, Tilted-axis precession and phase-sensitive detection of nuclear magnetization, J. Magn. Reson., Ser A 121 (1996) 8–22.

[38] H. Cho, Off-resonance multiple-pulse dynamics in solid-state NMR spectroscopy: a revised coherent averaging theory analysis, J. Magn. Reson. 141 (1999) 164–179.

[39] L. Mafra, C. Coelho, R. Siegel, J. Rocha, Assessing the performance of windowed ^{1}H CRAMPS methods, on biological solids, at high-field and MAS up to 35 kHz, J. Magn. Reson. 197 (2009) 20–27.

[40] S. Paul, R.S. Thakur, M. Goswami, A.C. Sauerwein, S. Mamone, M. Concistrè, H. Förster, M.H. Levitt, P.K. Madhu, Supercycled homonuclear dipolar decoupling sequences in solid-state NMR, J. Magn. Reson. 197 (2009) 14–19.

[41] M.E. Halse, L. Emsley, A common theory for phase-modulated homonuclear decoupling in solid-state NMR, PCCP 14 (2012) 9121–9130.

[42] S. Paul, P.K. Madhua, Homonuclear dipolar decoupling in solid-state nuclear magnetic resonance under the regime of moderate to high magic-angle spinning frequencies: Astatus report, J. Indian Inst. Sci. 90 (2012) 69–86.

[43] W.K. Rhim, Analysis of multiple pulse NMR in solids. II, J. Chem. Phys. 60 (1974) 4595.

[44] J.-P. Amoureux, B. Hu, J. Trébosc, Q. Wang, O. Lafon, F. Deng, Homonuclear dipolar decoupling schemes for fast MAS, Solid State Nucl. Magn. Reson. 35 (2009) 19–24.

[45] R.E. Marsh, A refinement of the crystal structure of glycine, Acta Crystallogr. A 11 (1958) 654–663.

[46] A. Lesage, D. Sakellariou, S. Hediger, B. Eléna, P. Charmont, S. Steuernagel, L. Emsley, Experimental aspects of proton NMR spectroscopy in solids using phase-modulated homonuclear dipolar decoupling, J. Magn. Reson. 163 (2003) 105–113.

[47] E. Vinogradov, P.K. Madhu, S. Vega, Proton spectroscopy in solid state nuclear magnetic resonance with windowed phase modulated Lee-Goldburg decoupling sequences, Chem. Phys. Lett. 354 (2002) 193–202.

[48] K. Yamauchi, S. Kuroki, I. Ando, The amide proton NMR chemical shift and hydrogen-bonded structure of glycine-containing peptides and polypeptides in the solid state as studied by multi-pulse-associated high-speed MAS ^{1}H NMR, J. Mol. Struct. 602 (2002) 9–16.

[49] M. Leskes, P.K. Madhu, S. Vega, A broad-banded z-rotation windowed phase-modulated Lee-Goldburg pulse sequence for ^{1}H spectroscopy in solid-state NMR, Chem. Phys. Lett. 447 (2007) 370–374.

[50] M. Leskes, P.K. Madhu, S. Vega, Supercycled homonuclear dipolar decoupling in solid-state NMR: toward cleaner H-1 spectrum and higher spinning rates, J. Chem. Phys. 128 (2008) 052309.

[51] F.M. Paruzzo, G. Stevanato, M.E. Halse, J. Schlagnitweit, D. Mammoli, A. Lesage, L. Emsley, Refocused linewidths less than 10 Hz in ^{1}H solid-state NMR, J. Magn. Reson. 293 (2018) 41–46.

[52] L. Stievano, F. Tielens, I. Lopes, N. Folliet, C. Gervais, D. Costa, J.-F. Lambert, Density functional theory modeling and calculation of NMR parameters: an ab initio study of the polymorphs of bulk glycine, Cryst. Growth Des. 10 (2010) 3657–3667.

[53] F.M. Paruzzo, B.J. Walder, L. Emsley, Line narrowing in ^{1}H NMR of powdered organic solids with TOP-CT-MAS experiments at ultra-fast MAS, J. Magn. Reson. 305 (2019) 131–137.

[54] Tom O'Haver, A pragmatic introduction to signal processing, https://terpconnect.umd.edu/~toh/spectrum/, 2019, July 1.

[55] E. Salager, J.N. Dumez, L. Emsley, M.H. Levitt, A scaling factor theorem for homonuclear dipolar decoupling in solid-state NMR spectroscopy, J. Magn. Reson. 212 (2011) 11–16.

[56] B. Elena, A. Lesage, S. Steuernagel, A. Böckmann, L. Emsley, Proton to carbon-13 INEPT in solid-state NMR spectroscopy, J. Am. Chem. Soc. 127 (2005) 17296–17302.

[57] U. Sternberg, R. Witter, I. Kuprov, J.M. Lamley, A. Oss, J.R. Lewandowski, A. Samoson, ^{1}H line width dependence on MAS speed in solid state NMR–comparison of experiment and simulation, J. Magn. Reson. 291 (2018) 32–39.

[58] L. Bosman, P.K. Madhu, S. Vega, E. Vinogradov, Improvement of homonuclear dipolar decoupling sequences in solid-state nuclear magnetic resonance utilising radiofrequency imperfections, J. Magn. Reson. 169 (2004) 39–48.

[59] A.J. Vega, Controlling the effects of pulse transients and RF inhomogeneity in phase-modulated multiple-pulse sequences for homonuclear decoupling in solid-state proton NMR, J. Magn. Reson. 170 (2004) 22–41.

[60] M. Leskes, P.K. Madhu, S. Vega, Proton line narrowing in solid-state nuclear magnetic resonance: New insights from windowed phase-modulated Lee-Goldburg sequence, J. Chem. Phys. 125 (2006) 124506.

[61] C. Coelho, J. Rocha, P.K. Madhu, L. Mafra, Practical aspects of Lee-Goldburg based CRAMPS techniques for high-resolution ^{1}H NMR spectroscopy in solids: implementation and applications, J. Magn. Reson. 194 (2008) 264–282.

[62] K.R. Mote, V. Agarwal, P.K. Madhu, Five decades of homonuclear dipolar decoupling in solid-state NMR: status and outlook, Prog. Nucl. Magn. Reson. Spectrosc. 97 (2016) 1–39.

[63] W.K. Rhim, D. Elleman, R. Vaughan, Analysis of multiple pulse NMR in solids, J. Chem. Phys. 59 (1973) 3740–3749.

[64] H.W. Spiess, H. Zimmermann, U. Haeberlen, Proton magnetic shielding and susceptibility effects in single crystals of ferrocene, Chem. Phys. 12 (1976) 123–130.

[65] E. Vinogradov, P.K. Madhu, S. Vega, A bimodal Floquet analysis of phase modulated Lee-Goldburg high resolution proton magic angle spinning NMR experiments, Chem. Phys. Lett. 329 (2000) 207–214.

[66] C. Filip, S. Hafner, Analysis of multiple-pulse techniques under fast MAS conditions, J. Magn. Reson. 147 (2000) 250–260.